Fast Charge Exchange Spectroscopy for Measurements of Ion-Velocity-Space Distribution Function

Mikirou YOSHINUMA[1)]*, Katsumi IDA[1)], Tatsuya KOBAYASHI[1,2)]

[1)] *National Institute for Fusion Science, National Institutes of Natural Sciences, Toki, Gifu 509-5292, Japan*
[2)] *The Graduate University for Advanced Studies, SOKENDAI, Toki, Gifu 509-5292, Japan*

(Received 5 August 2024 / Accepted 10 November 2024)

Fast charge exchange spectroscopy of C VI (Δn = 8−7, λ = 529.05 nm) has been developed to measure the ion-velocity-space distribution function. The fast charge exchange spectroscopy system consists of an F2.8 lens spectrometer, image intensifier, and high-speed camera. To maximize photon count, we efficiently accumulate light from 50 optical fibers (400 μm core) into one spatial channel. By applying a curved multi-slit, one spectrometer has four spatial channels. This system has good time resolution with a frequency of 10 kHz beyond that of ion-ion collision and excellent accuracy (signal-to-noise ratio), enough to detect the deformation of carbon ion-velocity distribution from Maxwell-Boltzmann distribution.

Keywords: charge exchange spectroscopy, ion-velocity distribution function, plasma diagnostic

DOI: 10.1585/pfr.19.1402037

1. Introduction

Charge exchange spectroscopy has been widely used to provide the radial profiles of ion temperature, toroidal and poloidal plasma flow velocity, and impurity and bulk-ion density [1–3]. It has a great advantage of providing local ion-velocity distribution at the intersection between a neutral beam and a line of sight. Typically, a charge exchange collision between hydrogen/deuterium atoms injected by a neutral beam and fully ionized carbon is used. In this analysis, the Maxwell-Boltzmann velocity distribution of ions is assumed. This is because the measurements' time resolution is typically lower than the ion-ion collision time scale, where time-integrated ion-velocity distribution becomes Maxwell-Boltzmann due to the collision process. Therefore, a high time resolution exceeding the ion-ion collision time scale is necessary to detect the deformation of ion-velocity distribution from Maxwell-Boltzmann distribution.

Recently, fast charge exchange spectroscopy has been developed [4]. However, the fluctuation of ion-velocity distribution has been treated as ion temperature and velocity fluctuation by applying Gaussian fitting to the spectrum measured. Increasing photon flux to reduce the noise level below the deformation level of ion-velocity distribution is also essential. In other words, the assumption of Maxwell-Boltzmann becomes necessary if the noise level is larger than the deformation of ion velocity, which is relatively small for bulk ions with velocities $v < 2v_{th}$, where v_{th} is thermal velocity. In order to realize both high time resolution and low photon statistical noise, the photon flux should be two orders of magnitude larger than that of conventional charge exchange spectroscopy. In this paper, the development of a fast charge exchange spectroscopy system with a high time resolution of 10 kHz and low enough noise to detect the deformation of the ion-velocity distribution from the Maxwell-Boltzmann distribution is described. In Sec. 2, the outline of this fast charge exchange system is described. The details of the curved multi-slit [5] that realizes multi-channel measurement are described in Sec. 3. Moment analysis of ion-velocity distribution is introduced in Sec. 4. In Sec. 5, an apparent offset of skewness and kurtosis due to applying a bandpass filter is discussed, using the example of the measurements of fast ion charge exchange spectroscopy. The moment analysis to quantify the deformation of ion-velocity distribution is described in Sec. 6.

2. Fast Charge Exchange Spectroscopy System

The fast charge exchange system consists of a lens spectrometer (Bunko-Keiki CLP-400), image intensifier (Hamamatsu unit C10880-13C), and high-speed camera (Photron FASTCAM Nova S6 16GB Type 800K-M-16GB), as shown in Fig. 1(a). The pixel size of the high-speed camera is 20 μm × 20 μm. We adapted a camera lens with a focal length of 400 mm and a F-number of 2.8, which gives two to five times larger photons than a conventional mirror spectrometer of similar focal length (*e.g.*, 300 mm F3.9 or 500 mm F6.5). The number of gratings is 2,160/mm, which gives a dispersion of 0.724 nm/mm at the exit of the spectrometer.

*Corresponding author's e-mail: yoshinuma.mikiro@nifs.ac.jp

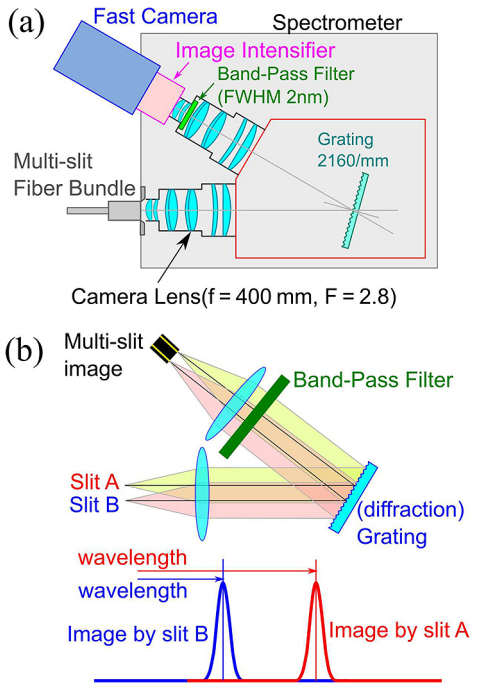

Fig. 1. Schematics of (a) spectrometer and (b) multi-slit of the fast charge exchange spectroscopy system for measurements of ion-velocity-space distribution function in LHD.

The horizontal magnification is 1.49. Since we need a large number of photons to improve the signal-to-noise ratio, 50 optical fibers (400 μm core) are arranged at the entrance slit for one spatial channel. The photocathode's diameter is 24 mm, and the image is reduced to 16 mm diameter at the fluorescent surface in the image intensifier unit and its magnification scale is 0.67. The 1:1 rely lens is used to transfer the image at the fluorescent surface to the detector surface of the high-speed camera. The dispersion at the fluorescent surface and at the detector of the high-speed camera is 1.09 nm/mm (0.0218 nm/pixel). The quantum efficiency of the photocathode is 10% at 530 nm. The short afterimage time of the fluorescent surface is also essential for high-time resolution measurements of 10 kHz. We selected P 46 as a fluorescent surface because it has an afterimage time shorter than ten microseconds. A multi-slit system is also adapted to have multi-channels in one spectrometer. Although only slits A and B are illustrated in Fig. 1(b), a four slit fiber bundle is installed at the entrance of the spectrometer, as described in Sec. 3. The image of slit A and slit B is transferred to the exit of the spectrometer in different wavelength position as shown in Fig. 1(b). The multi-slits cause the interference of the spectrum between adjacent slits. A bandpass filter with a full width at half maximum (FWHM) of 2 nm is installed inside the camera lens, where the light fluxes are parallel to eliminate this interference.

For applying the high-speed camera to the LHD experiments, it was operated to be the acquisition and storing were synchronized with the discharge. In LHD, the interval of discharges is relatively short, three minutes. The high-speed camera system waits of 30-second-before-discharge notification (minus 30-second signal). When the minus 30-second signal comes, the high-speed camera goes on standby and waits for the start trigger of 10 kHz of data acquisition. After archiving the data with a given frame number, vertical binning and data storage processes are performed before the next discharge. The maximum resolution of the high-speed camera is 1024(H) × 672(V) (H : horizontal, V: vertical) for the 10 kHz sampling and 640(H) × 480(V) for the 20 kHz sampling. The total memory is 16 GB, and the duration of the measurements for one discharge is 2.5 seconds. By increasing the memory size from 16 GB to 128 GB, the duration of the measurements can be extended up to 20 seconds. In this experiment, the region of interest (ROI) is set to 768(H) × 768(V), and the sampling time is set to 10 kHz for two seconds duration to complete data storage between the shot interval in LHD of three minutes. After acquisition, the data archived in the camera's memory is transferred to the PC. The data of each pixel is numerically integrated in the vertical direction to reduce the data size in storage. The data of each pixel of the high-speed camera is not stored, and only the signal integrated along the vertical direction is stored. In the case of vertical integration, the time from the end of measurement to its resumption was 153 seconds for data acquired with the 10 kHz 2.5 seconds (25,883 frames), which means that the speed was achieved in time for the next discharge in this experiment, in which the shot interval is 3 minutes (180 seconds). Because the integration process was performed in parallel with the data transfer, this time was almost that of the data transfer from the camera to the PC. In the case without vertical integration, the data size stored on the hard disk simply increased by a factor of the number of vertical pixels (768 pixels) compared to the vertical integration case, which increased the storage time.

3. Curved Multi-Entrance Slit for Spectral Smile Correction

Since the integration is performed along the vertical pixels of a high-speed camera, the wavelength of each pixel arranged in the vertical direction should be identical. Therefore it is necessary to correct the spectral smile where the wavelength of each pixel is shifted, depending on the height from the mid-plane of the slit. To correct the spectral smile and to make the wavelength shift from off mid-plane to zero, the curved multi-entrance slit is adapted. Figure 2(a) shows the arrangement of four sets of 50 optical fibers arranged along the slit curve designed to have a curvature of R = 326 mm which is calculated for the wavelength of 529.05 nm. The apertures of the 50 optical fibers (400 μm core) are used as an equivalent slit with 300 μm width and 21 mm height. The space between the adjacent slit is 3.4 mm, which corresponds to the wavelength separation of 3.67 nm, calculated by 3.4 mm × 1.49 (horizontal magnification) × 0.724 nm/mm.

Figure 2(b) shows the horizontal shift (in the wavelength direction) along the slit height for a straight entrance slit and a curved entrance slit, respectively. The horizontal

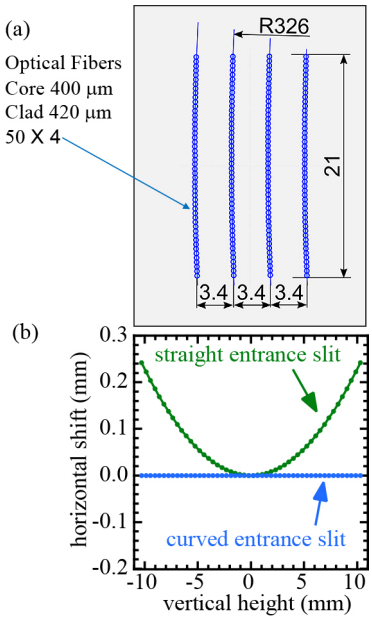

Fig. 2. (a) Curved entrance slit to straighten slit image on exit plane and (b) horizontal shift due to spectral smile of spectrometer.

shift reaches 0.24 mm (60% of the diameter of the optical fiber) at the edge of the straight entrance slit. In contrast, there is almost no horizontal for the curved entrance slit. The curved multi-entrance slit is quite a powerful technology to make the exit slit image straight and realize numerical pixel integration along the slit height before storing the data on the PC disk. This integration reduces the data size and writing time by almost three orders, which are essential issues for this diagnostic.

Figure 3 shows the observation position of the line of sight in a horizontally elongated poloidal section. Here the neutral beam of beamline five (BL5) is radially injected into the plasma, and the line of sight is in a toroidal direction. The fiber bundle of 104 (H) × 15 (V) with a 400 μm core and numerical aperture NA = 0.25 (F-number of 2) has been installed in LHD to cover the whole region of the plasma (R = 3.5–4.68 m) with spacing of ∼1.2 cm. The collection optic was constructed using a fixed-focal-length lens with an F-number of 2.8 and a focal length of 400 mm. The optical fibers are laid to the diagnostic room where the spectrometer was settled, and a panel with optical fiber connectors arranged in a one-to-one correspondence with the line of sight was installed. The region for the 50 optical fibers is arranged 5(H) × 10(V) and 6 cm × 12 cm in the poloidal cross-section. The spatial resolution of each channel is ∼6 cm in the radial direction with a vertical integration of z = ±6 cm. Due to the integration in the vertical direction, the effective spatial resolution becomes lower towards the plasma center. In this experiment, the radial location of ch1, ch2, ch3, and ch4 is 3.8, 4.0, 4.25, and 4.5 m, respectively. By changing the connection of optical fibers to the panel, one can easily select the region of the plasma to be measured.

The fiber image of these slits becomes a straight line by a simple correction with the curved multi-slit, as seen in Fig. 3.

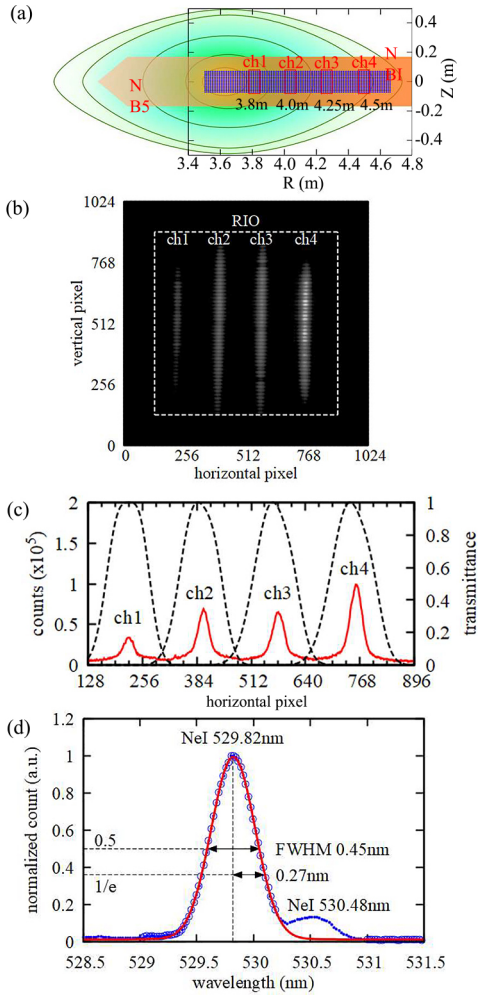

Fig. 3. (a) Setup of optical fiber at horizontally elongated plasma poloidal cross-section in LHD, (b) spectral image at exit plane of spectrometer, (c) spectrum of C VI (Δn = 8−7, λ = 529.05 nm) integrated along slit direction (closed circles + lines) and transmittance of bandpass filter (dashed lines), and (d) measured spectrum of Neon lamp (dot and circles) and line shape (529.819 nm) fitted with the Gaussian function (solid line).

Due to the numerical integration along the slit direction, the spectrum for each pixel is not stored, and only the spectrum for each slit is stored. Figure 3 shows the integrated signal along the slit direction. Because the bandwidth of the bandpass filter (2 nm) is smaller than the wavelength separation between the slit (2.5 nm), there is no interference of spectrum between the adjacent slits. The transmittance curves shown in Fig. 3(c) are obtained by measuring the light from a halogen lamp. Although there are overlapped regions on the filter curves, the non-overlapping range is 2.8 nm, which can be used for measuring C VI spectrum of T_i < 7 keV. The instrument width (0.45 nm in FWHM) is obtained by measuring the light from a neon lamp, as shown in Fig. 3(d). Spectrum of Ne I (529.82 nm) can be well-fitted with the Gaussian function indicated with a solid line by ignoring the spectrum around Ne I (530.48 nm).

4. Moment Analysis of Ion-Velocity Distribution

The moment analysis is a valuable tool for evaluating the contribution of a non-Maxwell component of the velocity distribution function quantitatively.

The distortion of ion-velocity distributions from Maxwell-Boltzmann distribution is evaluated quantitatively by using moment analysis of the charge exchange recombination spectra, which correspond to the ion-velocity distribution function.

The 0th, 1st, 2nd, and 3rd moments of the ion-velocity distributions are defined as

$$M_0 = \int f(v)dv, \tag{1}$$

$$M_1 = \frac{1}{M_0}\int v f(v)dv, \tag{2}$$

$$M_2 = \frac{1}{M_0}\int (v - M_1)^2 f(v)dv, \tag{3}$$

$$M_3 = \frac{1}{M_0 M_2^{\frac{3}{2}}}\int (v - M_1)^3 f(v)dv, \tag{4}$$

$$M_4 = \frac{1}{M_0 M_2^2}\int (v - M_1)^4 f(v)dv. \tag{5}$$

Here, M_0 corresponds to the number density of the species. When the velocity function $f(v)$ is Maxwell-Boltzmann distribution, each moment becomes $M_1 = V_s$, $M_2 = V_{th}^2/2$, $M_3 = 0$, $M_4 = 3$, where V_s and V_{th} are the projection of the flow velocity to the line-of-sight (mainly toroidal direction) and thermal velocity, respectively. Therefore, the finite values of skewness (M_3) and kurtosis (M_4-3) exceeding the noise level are clear evidence of distortion from the Maxwell-Boltzmann distribution. The skewness is an indication of the asymmetry of ion-velocity distribution. The kurtosis becomes positive when the ion-velocity distribution peaks more than the Gaussian profile. A moment as high as five is not detectable, and typically, the moment of ion-velocity distribution is evaluated up to four. The skewness is a good measure of the asymmetric distortion of velocity distribution from Maxwell-Boltzmann distribution in Landau damping.

5. Offset of Skewness and Kurtosis

Although the bandpass filter is useful to eliminate the interference of the spectrum between the slits, it causes apparent deformation of the spectrum from the Maxwell-Boltzman distribution. Figure 4 shows the effect of the bandpass filter on plasma flow (M_1), ion temperature (M_2), skewness (M_3), and kurtosis (M_4). Because there is no flat top of the transmission of the bandpass filter, it may cause an offset in plasma

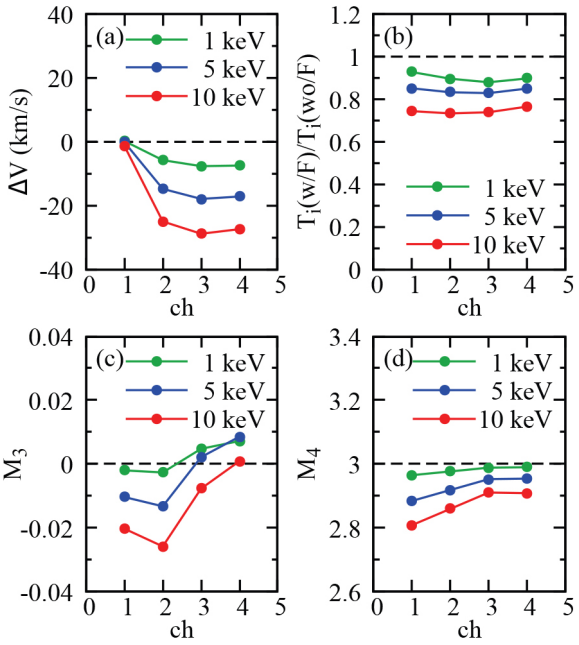

Fig. 4. Effect of bandpass filter: (a) shift of plasma flow (M_1), (b) ratio of ion temperature with filter to that without (M_2), (c) skewness (M_3), and (d) kurtosis (M_4).

flow. This offset becomes larger for ch2, ch3, and ch4, where the peak of the bandpass filter's transmission is shifted from the peak of the emission line. When the the peak of transmission of the bandpass filter matches the emission line, there is no offset as seen in ch1. The position of the incident slit affects the deformation of the filter characteristics due to the tilt of the light as it passes through the bandpass filter. The offset becomes larger as the ion temperature increases from 1 to 10 keV. The instrumental width (FWHM) is 0.45 nm, which corresponds to an ion temperature of ~1.5 keV. Because the FWHM of the bandpass filter is comparable to the Doppler width, the ion temperature evaluated from the spectrum with the filter is underestimated by 10–30%. The impact of the bandpass filter on the skewness (M_3) is small because the effect of the finite gradient of transmission curves affects only a low moment of (M_1). The apparent skewness due to the bandpass filter is less than 0.03, even for a high ion temperature of 10 keV. The impact of a bandpass filter on kurtosis is always negative because the bandpass filter cuts the wing of the spectrum. The decrease of kurtosis due to the bandpass filter is 0.2 at most, even for the 10 keV ion temperature.

In charge exchange spectroscopy, emission by electron impact and the charge exchange process with a thermal neutral becomes strong near the plasma periphery, called background emission or a cold component. To accurately measure plasma emission, we need to subtract the cold component. This is achieved by modulating the neutral beam, a process that allows us to isolate the background emission from the overall spectrum. Here, the cold component is unchanged in time even though the neutral beam is switched on or off. Because the thermal neutral increases slightly when the

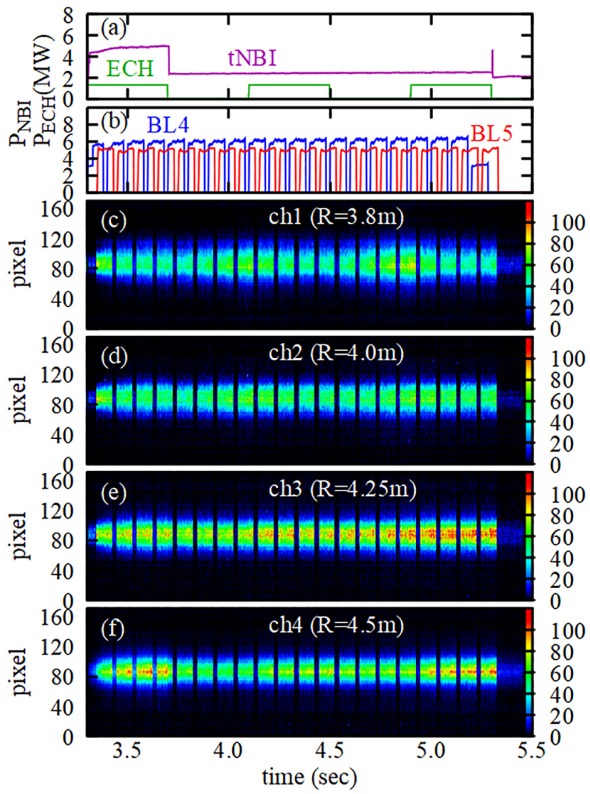

Fig. 5. Waveforms of (a) neutral beam injection (BL4: heating beamline & BL5: heating and probe beamline) and ECH pulses and contours of spectral intensity of (b) ch1, (c) ch2, (d) ch3, and (e) ch4, where y-axis of spectrum is pixel number (# 164229).

neutral beam is turned on, there is always a residual cold component. Therefore, it is essential to evaluate this apparent deformation of the spectrum from the steady-state discharge in which Gaussian profiles of ion-velocity distribution are expected. Since this apparent deformation is constant in time, it can be treated as an offset. Figure 5 shows the time evolution of the spectrum from ch1, ch2, ch3, and ch4 in the discharge where the BL4 and BL5 (probe beams) are modulated. It is clearly observed that the intensity of the spectrum is increased and decreased, associated with the on and off modulation of the BL5 to which the lines of sight are crossed. The spectrum at the beam on includes the background spectrum (cold component) and the moment analysis is applied to the spectrum produced by subtracting the background spectrum to see the skewness and the kurtosis in the standard discharge with Maxwell-Boltzmann ion-velocity distribution. Ion temperatures are measured with conventional CXS and are 2.6 keV, 1.8 keV, 1 keV, and 0.4 keV at the position of R = 3.8 m (ch1), 4.0 m (ch2), 4.25 m (ch3), and 4.5 m (ch4) respectively at 4 sec.

The skewness and kurtosis should be 0 and 3 in the Maxwell-Boltzmann distribution, respectively. To see the offset from the values in the Maxwell-Boltzmann, the radial profiles of time-averaged M_3 (skewness) and M_4-3 (kurtosis) for two seconds are plotted in Fig. 6. The standard error can be reduced by taking the average (with 15,597 frames for Fig. 6), although the standard deviation of M_3 and M_4 are 0.14

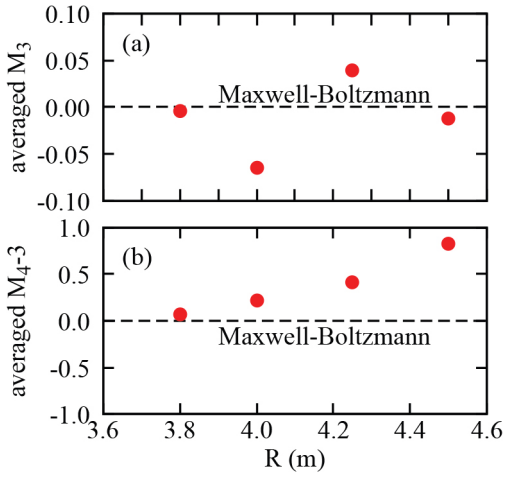

Fig. 6. Radial profiles of time-averaged (a) skewness M_3 and (b) kurtosis M_4-3 (# 164229).

and 0.28 respectively during the steady-state discharge. The skewness, a crucial parameter in our study, offset of ch2 is 0.07, and this is notably larger than the bandpass filter's effect (0.03). In stark contrast, the offset of the kurtosis, a key parameter, increases toward the plasma periphery, where the contribution of the residual cold component becomes large. The subtraction of cold components becomes less perfect in the peripheral region due to an increase of cold components with the NB injection. This positive offset of kurtosis is primarily caused by the cold component, whose Doppler width is narrower than that of the charge exchange component, leading to this distinct effect. The kurtosis offset near the plasma center (R = 3.8 m) is small. However, the kurtosis offset increases towards the plasma edge and reaches 0.8 at R = 4.5 m, much larger than the bandpass filter's effect (0.2). The cold component's effect on the kurtosis is dominant, and the bandpass filter's impact is negligible. Therefore, the influence of a nonflat bandpass filter transmission curve can be negligible in estimating skewness and kurtosis. By focusing on the time changes in skewness and kurtosis during an event that causes distortion, it is possible to investigate how the distortion changes, although there is an offset in skewness and kurtosis.

6. Deformation of Ion-Velocity Distribution from Maxwell-Boltzmann Distribution

The deformation of ion-velocity distribution from the Maxwell-Boltzmann distribution is observed transiently associated with a large MHD burst excited at the plasma edge characterized by a magnetic field oscillation with large amplitude, an abrupt drop in neutron emission, and sharp spikes of RF intensity. This MHD burst is one of the helically trapped energetic particle-driven instabilities triggered by a tongue collapse [6–8]. The deformation of the ion-velocity distribution is due to the energy transfer from the wave to the bulk-ion particles through Landau and the transit-time damping of the large-amplitude MHD wave [9, 10].

Figure 7 shows the time evolution of neutral beam power, the magnetic probe signal, the neutron emission rate, RF intensity measured with RF probe, and contour of spectral before the background subtraction measured with high-speed charge exchange spectroscopy at R = 4.0 m (ch2), 4.25 m (ch3), and 4.5 m (ch4). The neutral beam BL5 is the probe beam for charge exchange spectroscopy, and the background emission (cold component) is obtained in the period between the NBI gap. The amplitude of magnetic perturbation reaches 0.2 mT, which is almost one order of magnitude larger than a typical MHD oscillation. The sharp drop in neutron emission rate is due to the energy transfer from energetic particle to wave and radial diffusion of energetic particles. The gradual decrease of the neutron emission rate between the NBI gap is due to the slowing down of energetic particles injected by BL4 and BL5. The RF intensity is the measure of ion loss at the plasma edge, which excites instability at a frequency range of a few hundred MHz to a few GHz. Since the increase of RF intensity, taken with a sampling time of 0.01 msec, is extremely sharp (within 0.2 msec), as shown in Fig. 7(h), this signal is used as a reference timing of the onset of the MHD burst for conditional spectrum averaging.

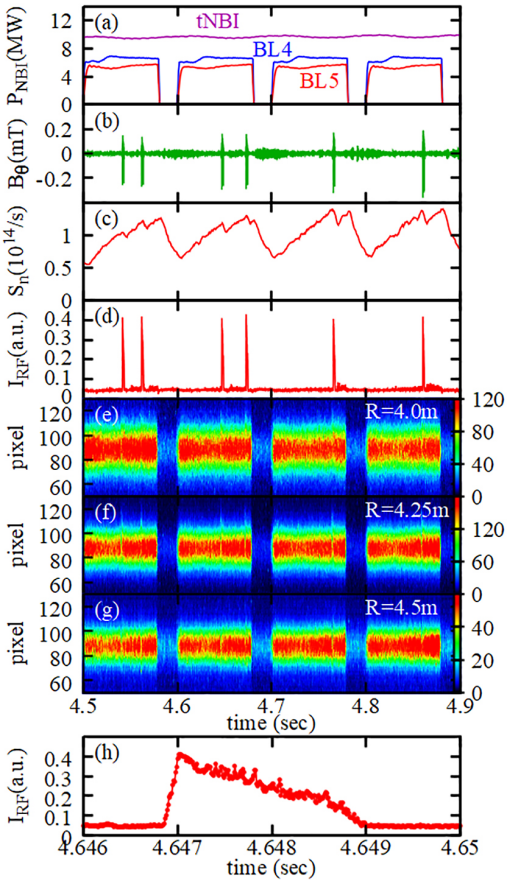

Fig. 7. Time evolution of (a) neutral beam power (tangentially injected NB: purple, BL4: blue; BL5: red), (b) magnetic perturbation, measured with magnetic probe, (c) neutron emission rate measured with fission chamber, (d) 880 MHz RF intensity measured with RF probe, and contours of spectral intensity of C VI (Δn = 8−7, λ = 529.05 nm) at (e) R = 4.0 m, (f) R = 4.25 m, and (g) R = 4.5 m (# 175364). (h) A time expanded view of RF intensity.

Figure 8 shows the spectrum of C VI (529.05 nm), which corresponds to the carbon ion-velocity distribution, measured at 4.76505, 4.76515, and 4.76525 sec (10 kHz sampling) and the conditional spectrum averaging spectrum for R = 4.0, 4.25, and 4.5 m. In this discharge, there were seventeen events of MHD burst, and the 17 spectra are averaged with respect to the rise of the RF spike. The jagged structure seen in the original spectrum is simply due to photon noise because the width of it is smaller than the instrumental width. The S/N becomes less at the edge (R = 4.5 m) where the amount of the fully ionized carbon is small. The noise seen in the original spectrum disappears by the conditional spectrum averaging, especially in the spectrum at R = 4.25 m. The spectrum at R = 4.25 m and Δt = 0.1 ms shows a clear gradient decrease (flattening) at λ = 529.4 nm. This deformation of carbon ion-velocity distribution is due to the simultaneous increase of population for λ > 529.4 nm and the decrease of population for λ < 529.4 nm. This is called a bipolar signature and is evidence of Landau and time-transit damping. The bipolar signature is most significant at R = 4.25 m, where the MHD burst starts. The wavelength of the pivot point of 529.4 nm ($\Delta\lambda$ = 0.35 nm) corresponds to a phase velocity of ~200 km/s. The deformation occurs within 0.1 ms and mainly appears at the Doppler velocity, where the phase velocity of the MHD burst matches. The order of the ion-ion collision time is 10^{-3} sec for carbon impurity ions and 10^{-2} sec for bulk ions in this plasma.

The skewness and kurtosis are good measures for evaluating the deformation of ion-velocity distribution from Maxwell-Boltzmann distribution. Figure 9 plots the time evolution of the first, second, third, and fourth moments of the carbon ion-velocity distribution function. The first moment of the ion-velocity distribution is toroidal plasma flow velocity of carbon impurity, and the positive value corresponds to the

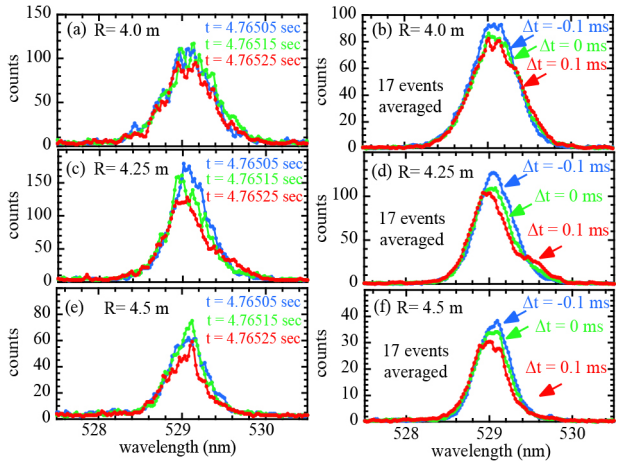

Fig. 8. Spectrum of C VI (Δn = 8−7, λ = 529.05 nm) for (a) ch2 (R = 4.40 m, r_{eff}/a_{99} = 0.67), (c) ch3 (R = 4.25 m, r_{eff}/a_{99} = 0.93), and (e) ch4 (R = 4.5 m, r_{eff}/a_{99} = 1.12) at t = 4.76505, 4.76515, 4.76525 sec from single event, and (b)(d)(f) averaged spectrum with 17 events, where Δt is time respect to onset of MHD burst (# 175364).

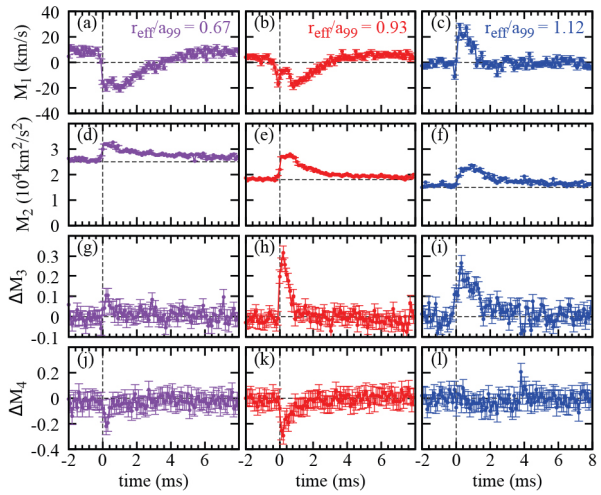

Fig. 9. Time evolution of (a)(b)(c) 1st, (d)(e)(f) 2nd, (g)(h)(i) 3rd, and (j)(k)(l) 4th moment of ion-velocity distribution function as function of time with respect to onset of MHD burst defined by jump of RF intensity for (a)(d)(g)(j) ch2 (R = 4.0 m, r_{eff}/a_{99} = 0.67), (b)(e)(h)(k) ch3 (R = 4.25 m, r_{eff}/a_{99} = 0.93), and (c)(f)(i)(l) ch4 (R = 4.5 m, r_{eff}/a_{99} = 1.12) (# 175364).

toroidal rotation parallel to the equivalent plasma current (co-direction). In contrast, the negative one corresponds to the toroidal rotation anti-parallel to the equivalent plasma current (counter-direction). In the toroidal plasma, it rotates in the counter-direction when the plasma potential becomes negative due to the ion loss. Therefore, the change in the first moment to negative value inside the LCFS ($r_{eff}/a_{99} < 1$) and positive value outside the LCFS ($r_{eff}/a_{99} > 1$) indicates the ion loss across the LCFS. This is consistent with the fact that the RF probe shows the sudden onset of edge instability excited by the ion loss across the LCFS.

The increase in the second moment is due to the energy transfer from wave to carbon ion through Landau and transit-time damping. The increase is abrupt and occurs within 0.1 ms. It should be noted that this time scale is much smaller than that of ion-ion collisions of carbon and much shorter than that of heating by a collision process. The increase is due to the collisionless energy transfer from wave to particle via Landau and transit-time damping of the MHD wave. The abrupt change in skewness and kurtosis indicates that the carbon ion-velocity distribution deforms at the onset of the MHD burst (t = 0). This deformation of ion-velocity distribution is most significant at $r_{eff}/a_{99} = 0.93$, as the MHD burst starts. The jump of skewness is 0.3, which is one order of magnitude larger than the noise level comparable to the effect of the bandpass filter (0.03). The drop of kurtosis is also 0.3, which indicates that the carbon ion-velocity distribution becomes less peaked and is also observed at $r_{eff}/a_{99} = 0.93$. These changes in skewness and kurtosis strongly suggest the occurrence of Landau and transit-time damping, in which the flattening of the ion-velocity distribution at the resonance phase velocity is expected [9]. The deformation of the ion-velocity distribution disappears within 1–2 ms due to the ion-ion collision. As seen in the change in skewness at $r_{eff}/a_{99} = 1.12$, the deformation of the carbon ion-velocity distribution propagates outwards even outside the LCFS.

7. Summary

The key issues for measuring the ion velocity-space distribution function are high time resolution below the ion-ion collision time and low noise level below the deformation of the Maxwell-Boltzman distribution. The spectrometer requires a large aperture and high photon throughput to realize the high time resolution and the low noise level. The aperture size is a total of the 50 optical fibers (400 μm) for one spatial channel, and a lens spectrometer with F/2.8 is used. The system consists of many optical fibers and a lens spectrometer, an image intensifier, and a high-speed camera. The critical technology of fast charge exchange spectroscopy is a curved multi-entrance slit which makes the data size small and data writing time short of realizing this fast charge exchange spectroscopy.

Fast charge exchange spectroscopy for carbon impurity has been installed in LHD and applied to measure the deformation of carbon ion-velocity distribution from Maxwell-Boltzman distribution, which is characterized by finite skewness and finite kurtosis-3. The time evolution of skewness and kurtosis at the MHD event demonstrates the deformation of carbon ion-velocity distribution due to Landau and transit-time damping and the propagation of its deformation to the plasma edge. The direct measurement of the ion-velocity distribution function enabled by fast charge exchange spectroscopy underscores its potential as a powerful tool. This tool can significantly enhance our understanding of phase space (velocity and real space) fluctuation and dynamics in magnetically confined plasma.

Acknowledgments

The authors are grateful to the technical staffs of LHD for their excellent support for this work which is supported by the National Institute for Fusion Science grant administrative budgets (NIFS10ULHH021) and JSPS KAKENHI Grant Numbers JP21H04973. The datasets generated during and/or analyzed during the current study are available in the Large Helical Device (LHD) data repository server of the National Institute for Fusion Science (NIFS) at https://doi.org/10.57451/lhd.analyzed-data.

[1] M. Yoshinuma *et al.*, Fusion Sci. Technol. **58**, 375 (2010).
[2] K. Ida *et al.*, Plasma Fusion Res. **14**, 1402079 (2019).
[3] K. Ida *et al.*, Rev. Sci. Instrum. **90**, 093503 (2019).
[4] M. Cavedon *et al.*, Rev. Sci. Instrum. **88**, 043103 (2017).
[5] R.W. Esplin, Optical Engineering **19**, 623 (1980).
[6] K. Ida *et al.*, Sci. Rep. **6**, 36217 (2016).
[7] K. Ida *et al.*, Sci. Rep. **8**, 2804 (2018).
[8] S. Voermans *et al.*, Nucl. Fusion **59**, 106041 (2019).
[9] K. Ida *et al.*, Commun. Phys. **5**, 228 (2022).
[10] Y. Kawachi *et al.*, Rev. Sci. Instrum. **94**, 103505 (2023).